MINERVA: A facility to study Microstructure and INterface Evolution in Realtime under VAcuum

Chris Nicklin, Josue Martinez-Hardigree, Adam Warne, Stephen Green, Martin Burt, John Naylor, Adam Dorman, Dean Wicks, Salahud Din, and Moritz Riede

Citation: Review of Scientific Instruments **88**, 103901 (2017); doi: 10.1063/1.4989761
View online: http://dx.doi.org/10.1063/1.4989761
View Table of Contents: http://aip.scitation.org/toc/rsi/88/10
Published by the American Institute of Physics

MINERVA: A facility to study Microstructure and INterface Evolution in Realtime under VAcuum

Chris Nicklin,[1,a)] Josue Martinez-Hardigree,[2,b)] Adam Warne,[1] Stephen Green,[1] Martin Burt,[1] John Naylor,[3] Adam Dorman,[3] Dean Wicks,[3] Salahud Din,[3] and Moritz Riede[2]
[1]*Diamond Light Source, Ltd., Harwell Science and Innovation Campus, Chilton OX11 0DE, United Kingdom*
[2]*Clarendon Laboratory, University of Oxford, Oxford OX1 3PU, United Kingdom*
[3]*Kurt J. Lesker Company, Hastings TN35 4NR, United Kingdom*

(Received 12 June 2017; accepted 11 September 2017; published online 2 October 2017)

A sample environment to enable *real-time* X-ray scattering measurements to be recorded during the growth of materials by thermal evaporation in vacuum is presented. The *in situ* capabilities include studying microstructure development with time or during exposure to different environmental conditions, such as temperature and gas pressure. The chamber provides internal slits and a beam stop, to reduce the background scattering from the X-rays passing through the entrance and exit windows, together with highly controllable flux rates of the evaporants. Initial experiments demonstrate some of the possibilities by monitoring the growth of bathophenanthroline (BPhen), a common molecule used in organic solar cells and organic light emitting diodes, including the development of the microstructure with time and depth within the film. The results show how BPhen nanocrystal structures coarsen at room temperature under vacuum, highlighting the importance of using real time measurements to understand the as-deposited pristine film structure and its development with time. More generally, this sample environment is versatile and can be used for investigation of structure-property relationships in a wide range of vacuum deposited materials and their applications in, for example, optoelectronic devices and energy storage.
https://doi.org/10.1063/1.4989761

I. SCIENTIFIC MOTIVATION AND BACKGROUND

A key focus of materials science is the study of structure-property relationships, in which macroscopic properties often arise hierarchically from atomic interactions through mesoscale ordering. Common examples include the dependence of mechanical strength of a polycrystalline metal on its constituent grain size[1] or the modification of catalytic activity with film thickness or surface area.[2] Similar relationships frequently play a role in photovoltaic devices based on emerging energy materials, such as charge-transfer dyes, organic semiconductors, and organometal halide perovskites. Structurally dependent parameters such as charge carrier mobility, electronic band structure, or molecular orientation have been shown to have a direct influence on power conversion efficiency.[3,4] Several fabrication techniques have been used to explore the effect of processing on structure-property relationships, including solution-based slot-die coating and ink-jet printing,[5] as well as vacuum deposition,[6] the latter an increasingly popular tool as a method for fabricating large area electronic devices with fine control over nanoscale thickness, deposition rate, and composition. There are two main drawbacks of investigating post-deposition films: (a) it is challenging to identify interface effects during the growth and resolve variations in microstructure at different depths inside the film, though both can be critical for the performance of devices made from such films; (b) that many emerging materials are susceptible to degradation or morphological evolution from ambient moisture or oxygen[7–9] or even illumination.[10] As a consequence, *ex situ* investigations in which samples must be transferred through air, as is the case with many systems for atomic force microscopy (AFM), scanning and transmission electron microscopy (SEM, TEM), or laboratory based X-ray scattering, may create the additional challenge of relating measurements taken hours or days after fabrication to the structures captured in encapsulated, device-processed materials. *In situ* techniques are needed to capture film growth as it proceeds during real-world device processing.

The high flux of X-rays available at a synchrotron source means that high quality, low noise structural data can be collected very quickly. This has been recognised in the growing application of synchrotron radiation to *real-time* measurements of vacuum-deposited thin films fabricated with a wide range of deposition techniques including sputtering,[11–14] chemical vapour deposition,[15] molecular beam epitaxy,[16,17] and organic vapor-jet deposition.[18] Such scattering measurements are complementary to local structure measurements with AFM, as the elongated footprint of the X-ray beam at grazing angles probes the statistical average structure over a large area. Information such as the degree of crystallinity of the film, surface roughness, and domain size in polycrystalline regions and evidence of lattice strain or preferred orientation can be probed with high spatial and time resolution. Moreover, these parameters can be probed as a function of growth conditions such as substrate temperature, deposition rate, or the

[a)]chris.nicklin@diamond.ac.uk
[b)]josue.martinezhardigree@physics.ox.ac.uk; Joint first author.

pre-deposition of a buffer or templating layer. It is also possible to monitor the development of the film structure with time, with exposure to a specific gas or in an atmospheric pressure of air (due to the penetrating nature of X-rays).

Research into emerging energy materials is progressing across several materials and device architectures, from organic bulk heterojunctions to planar perovskite absorbers, and with many solution-based fabrication techniques spanning spin-casting,[19] blade-coating,[20–22] and ink-jet printing.[5] However, vacuum deposition is increasingly popular as a scalable method for fabricating large area electronic devices with fine control over nanoscale thickness, deposition rate, and ambient composition.[6] Here we present an environmental chamber specifically designed and optimised for the grazing incidence wide angle X-ray scattering (GIWAXS) or grazing incidence small angle X-ray scattering (GISAXS) study of *in situ* vacuum deposited layers on the synchrotron beamline I07,[23] at Diamond Light Source.

II. DESIGN CONSIDERATIONS AND CONSTRAINTS

GIWAXS and GISAXS are techniques where an X-ray beam hits a sample at grazing angles, close to the critical angle for total external reflection ($\sim 0.1^\circ$ for most organic materials at typical X-ray energies of ~12.5 keV). The scattered X-rays are collected using a large area two-dimensional detector to image the full scattering pattern in both the in-plane and out-of-plane directions (perpendicular and parallel to the sample normal, respectively). The implementation available at beamline I07 uses a Pilatus P2M detector mounted at a distance of ~300 mm for GIWAXS (or up to 3 m for GISAXS) from the sample to give a potential angular collection range of up to 40°. The use of a flat detector introduces some geometrical distortions at such small distances that must be corrected to remap the pixels to the true momentum transfer values (q_{xy} and q_z). Many sample environments exist that have been developed to study pre-grown samples and optimise the signal to noise for weakly scattering samples such as for organic photovoltaic (OPV) bulk heterojunction (BHJ) structures. They can generally incorporate a flowing gas to reduce air scattering or prevent oxidation/degradation of the interface during the X-ray measurements. We utilise similar design principles for our vacuum system, by incorporating elements such as internal pre-sample slits and a post-sample beam stop, to reduce the background caused by the incoming or exiting X-ray beam hitting the window material of the sample environment.

An additional constraint in the design is the requirement for the evaporation sources (to vacuum deposit the materials) to point upwards. Two sources need to be incorporated, to enable studies of application relevant interfaces as well as the growth of binary mixtures. In order to provide a versatile and accurate system, the design also includes two Quartz Crystal Microbalances (QCMs) for independent monitoring of the evaporating fluxes, allowing co-evaporation of materials. Other requirements are a sample shutter and a sample transfer system to limit the changeover time between experiments as well as a heatable substrate stage. To undertake the measurements, it is necessary to have accurate control over the sample motion, both the translations and rotations about the sample position. Beamline I07[23] is a beamline for grazing incidence and surface diffraction studies, which uses a high precision hexapod for sample alignment and a large diffractometer for complex multicircle positioning. In the GIWAXS studies, the P2M detector is fixed to the diffractometer detector circles, and the sample does not need the full range of motions provided by the diffractometer. Therefore in order to produce a stable platform for the GIWAXS studies, a frame that fits onto the diffractometer base has been implemented with all sample movement then provided via the hexapod. During GISAXS measurements, the same sample manipulation is used, and the P2M detector sits on an independent positioning platform downstream of the diffractometer.

III. IMPLEMENTATION

A. General arrangement

The general arrangement of the chamber is shown in Fig. 1, whilst a cut-through view of the chamber is shown in Fig. 2. The MINERVA (Microstructure and INterface Evolution in Realtime under VAcuum) system is designed to meet the design criteria and consists of four different sections:

(1) The lower deposition chamber contains the evaporation sources and QCMs. MINERVA's overall arrangement is dictated by the requirement for the evaporation sources to be upward pointing, to enable a constant evaporation rate through material covering the base of the crucible. They also operate at an optimum throw distance of 230 mm between the source and the sample position, ensuring an even flux over the sample area. This chamber also houses two QCMs to independently measure the flux rates of the two materials and a baffle between the deposition sources to ensure no cross talk in the

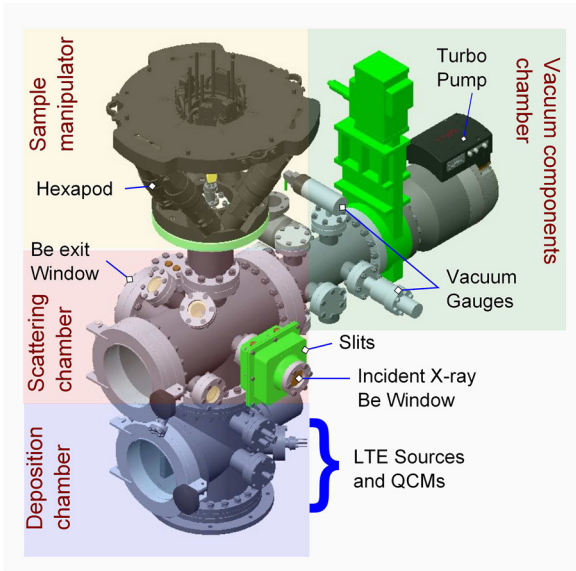

FIG. 1. Overview of the design of the MINERVA chamber. It consists of four modules: the deposition chamber houses the low temperature evaporation (LTE) sources and quartz crystal microbalances (QCMs); the scattering chamber with beryllium windows and slits; the sample manipulator using an external hexapod to allow accurate positioning of the sample; the vacuum component chamber with all pumps, gauges, and valves.

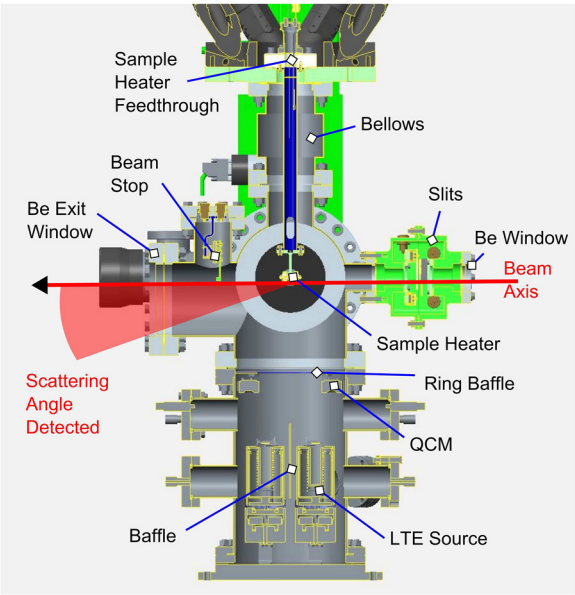

FIG. 2. Cut-through of the MINERVA chamber looking from the front (access ports), showing key internal components and the path of the X-ray beam.

flux calibrations. A separate ring baffle at the top of the base chamber protects all components above from being coated with an evaporating material, except for the substrate.

(2) The central scattering chamber houses the X-ray transparent beryllium entrance and exit windows. It also contains a set of pre-sample slits to define the X-ray beam and a post-sample beam stop, so that any unscattered beam does not add to the background levels (see Sec. III C). This chamber also provides an automated sample shutter which prevents deposition onto the sample during initial evaporator configuration and warmup.

(3) The upper sample manipulator consists of a hexapod external to the vacuum, the motions of which are fed into the vacuum chamber via a flexible vacuum bellows and feedthrough. The stage, incorporating the sample heater assembly, reaches down into the centre of the scattering chamber.

(4) The vacuum component chamber contains the pumping and ancillary services (venting, gauges), mounted on a multiport vessel that is at the rear of the system when it is mounted on the diffractometer available at beamline I07.[23] As GIWAXS/GISAXS measurements do not require substantial movement of the diffractometer, this allows short, simple cable and pipework management to common electrical controller and backing pump locations.

MINERVA is built in a very modular way, to enable flexibility in the studies for which it can be used. It allows, for example, replacement of the bottom chamber with another design that may contain different types of vacuum deposition sources. In addition, it would be possible to combine the X-ray scattering measurements with other related techniques by modifying the upper scattering chamber. The current implementation includes four flanged ports with the two smaller ports optically centred on the substrate position. These are currently used for video monitoring of the sample during alignment and deposition but could be used for introducing various kinds of probes to the sample. Although the system in its current configuration does not have optical viewports set at 74° for *in situ* spectroscopic ellipsometry, a technique which has been successfully combined with GIXD measurements,[24] the available ports could accommodate fibre-optic feedthroughs for complementary optical techniques such as *in situ* differential reflectance.[25,26] In addition, connections for enabling electrical measurements of films in organic field-effect transistors (OFETs) during or after deposition[27,28] can be easily integrated using the current flange ports.

B. Deposition chamber

The lower deposition chamber contains two low temperature evaporator (LTE) sources (Kurt J. Lesker Company) with individual flip shutters and power supplied through a common electrical feedthrough flange. Their temperature range of up to 600 °C is sufficient for depositing the organic materials used in OPVs. The sources are mounted directly on the base flange with a baffle placed between them to remove any temperature cross talk or cross contamination of the sources and to ensure that the flux rates correspond only to the specific source. This design allows very accurate studies of two component material systems where the relative composition of the two components can affect both the structure and the photovoltaic efficiency of the sample. Separate QCMs record the flux rates of the evaporants, enabling complex heterojunctions to be produced. This may include growing a single component wetting layer before a two-component material is deposited as required, for example, in many BHJ structures of OPVs. The flux rates can be calibrated before the deposition, as the sample is protected by a pneumatically operated shutter. This acts off one of the ports in the central scattering chamber, and the pneumatic actuator rotates to either place a steel plate in the path of the evaporating materials (but not blocking the X-ray path to enable alignment of a clean sample) or completely removing it out of the way. This shutter can be actuated remotely allowing the initial stage dynamics (e.g., nucleation, wetting behaviour, or strain development) to be monitored during the deposition.

C. Scattering chamber: X-ray background reduction

The quality of the GIWAXS/GISAXS measurement is critically dependent on the signal to noise ratio, as there are very many weak signals that are important to fully understand the structure of the developing interface. The measurements typically use an X-ray incidence angle very close to the critical angle for total external reflection (typically 0.1° for most organic materials at X-ray energies of ~12.5 keV). A well defined X-ray beam is therefore required and I07 has beam parameters of ~80 μm vertically by ~120 μm horizontally. The vertical size will flood the sample at 0.1° when the sample has a diameter of ~10 mm, but even then a strong reflected beam can lead to background scattering. Much of the background scattering originates from the intense X-ray beam hitting either the entrance or exit window of the sample environment. In

a vacuum chamber, these windows are generally made from polycrystalline beryllium that leads to some powder diffraction but also has a grain structure leading to small angle scattering close to the direct beam. In order to reduce the amount of this scattering reaching the detector, we borrow ideas from non-vacuum GIWAXS sample environments where the beam definition slits are after the entrance window and an internal beam stop is located to prevent the direct beam or reflected beam from hitting the exit window. This combination blocks the majority of the unwanted scattering that would reach the detector, cleaning up the signal significantly. It is important that the slits are high precision to define an accurate beam size and the beam stop can be reliably moved and relocated in order to enable initial alignment that is usually performed on an attenuated direct X-ray beam. This implementation makes use of in-vacuum stages incorporating SmarACT-precision linear drives (travel range of 10 mm and nm precision) in both the slits and the beam stops. Figure 3 shows the slit arrangement that uses four separate linear drives, each attached to one blade of the slits. These are software coupled to allow the gap and position of the slit to be set directly. The slits are mounted within a custom designed housing that splits to allow easy maintenance of the individual slit pairs. They join together using an O-ring mechanism that is compressed by a series of bolts through the external part of the housing. The slits mount directly onto the flange of the chamber, and a small Be window is mounted on the upstream side as indicated in Fig. 2. This combination serves two purposes: to define a small beam onto the sample and to block the front window X-ray scattering.

The beam stop assembly is constructed from two SmarACT stages mounted perpendicular to each other to provide an XY motion with a travel range of ±10 mm. The beam stop (see Fig. 4) mounts directly onto these stages and is designed so that it nominally blocks the beam at the centre of travel in both directions. The beam stop is made from 3 mm tungsten in order to ensure blocking of the intense direct beam when required

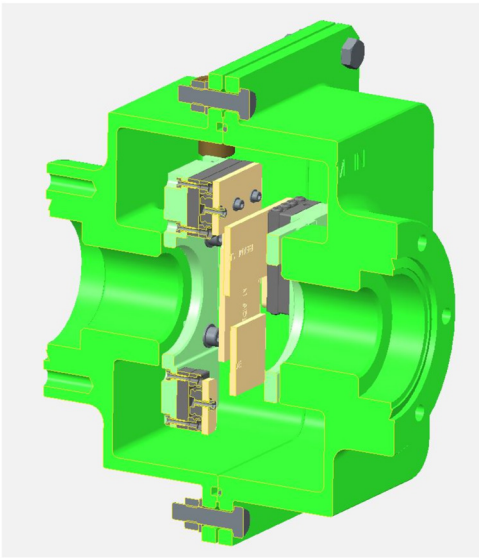

FIG. 3. Cut-through of the internal slit assembly. The slits are highlighted in yellow and allow the vertical and horizontal widths of the beam to be adjusted.

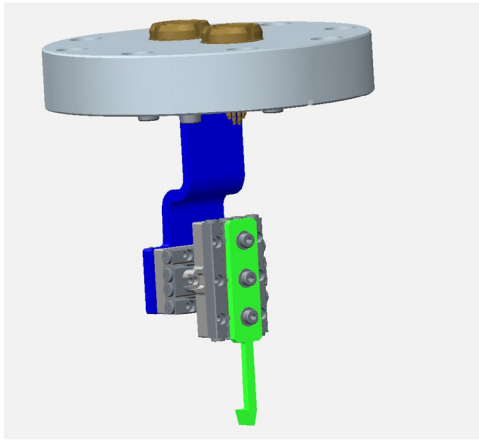

FIG. 4. The internal tungsten beam stop assembly is mounted after the sample with respect to the incoming X-ray beam. It allows cutting out the intense direct beam or the direct and reflected beam without blocking too much of the scattered signal.

and is arrow shaped to allow selective blocking of the direct beam or the direct and reflected beam without shadowing too much of the GIWAXS scattering.

D. Sample manipulator: Sample motion and heating

There are limited requirements for sample motion in the GIWAXS/GISAXS measurements; there must be vertical motion to position the sample accurately in the X-ray beam and angular motion of a few degrees to flatten the sample in two orthogonal directions and to set the beam incidence angle. We implement all of these motions using a hexapod directly attached to the sample through a vacuum feedthrough and a flexible edge welded bellows. An internal tube mounts off the flange and passes down to the sample heater assembly with the cabling routed axially along the hexapod to prevent cable snagging. In these experiments, there is no requirement for azimuthal rotation although this could be added using either an internal rotation stage or a differentially pumped rotary seal attached to the bellows. A hexapod provides a number of advantages for the sample positioning, the most significant of which is the ability to define the rotational pivot point, allowing optimal alignment even if the beam height entering the chamber is varied. In addition, the hexapod allows translation across the sample surface during the measurements which can be important when determining the role of beam damage on structural degradation. It should be noted that the hexapod local Cartesian axes must be correctly aligned parallel (and perpendicular) to the beam direction to ensure accurate calibration of the incidence angle.

The design of the sample heater is shown in Fig. 5. It uses resistive heating from a Nichrome wire threaded through a machinable ceramic assembly, allowing sample temperatures of up to ~600 °C. The Nichrome wire is used to provide compatibility with heating in a non-vacuum environment that may be required for certain sample processing or to study the effects of gas exposure on sample structure. The heater is controlled via a Eurotherm 2504 controller using feedback from the K-type thermocouple mounted as close to the sample position as possible. Samples are mounted on Omicron flag type sample

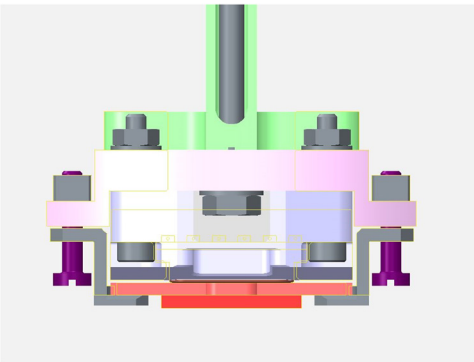

FIG. 5. Cut-through of the sample heater assembly. The upper section (green) shows the substrate coupling that attaches to the alignment hexapod, whilst the pink section and purple fixtures indicate the spring loaded sample clips that hold the transferable sample holders rigidly during measurement. The blue section is the machinable ceramic heater, housing a Nichrome heating wire to enable heating in oxygen or ambient atmospheres. The transferable sample plate and sample are shown in red.

plates that can be inserted either individually through the upper access door or by replacing the upper door (see Fig. 1) with a customised cluster flange that contains a sample transfer wobble stick, a sample carousel for storage of up to twelve samples, and viewing windows to enable simple sample transfers. This reduces the time between experiments significantly, and the only extended changeovers occur when evaporant materials need to be exchanged.

E. Vacuum component chamber: Vacuum control

The base vacuum required during deposition, in a production relevant process, is $<1 \times 10^{-6}$ mbar so it is not necessary to bakeout the chamber. This also enables a number of different flange sealing techniques to be used. Where compatibility with other ultrahigh vacuum (UHV) beamline equipment is required, conflat flanges are used where a knife edge cuts into a copper gasket, but in other places O-rings are used with compression fittings. The chamber is pumped via a combination of a backing line scroll pump and a 330 l/s turbomolecular pump (TMP), whilst pressure measurement is provided via a combination of a Pirani gauge for low vacuum and an Inverted Magnetron Gauge (IMG) for the higher vacuum. Initial pumpdown is achieved by closing a pneumatic valve between the backing pump and the turbomolecular pump and opening a bypass valve to pump the main chamber. At a pressure of 10^{-2} mbar, the bypass line valve is automatically closed and the valve to the TMP backing line is opened. The main valve between the TMP and the chamber is then opened, allowing the vacuum to rapidly reach the required level. The ultimate vacuum achieved is $\sim 5 \times 10^{-8}$ mbar after 2 h of pumping, which is more than adequate for deposition of these molecular species.

Control of the vacuum system is undertaken using a programmable logic controller (PLC) that allows the sequence above to be performed automatically at the touch of a button on a pressure sensitive screen, whilst monitoring the vacuum interlocks for safety and equipment protection. The PLC controls electronically actuated valves to ensure that a consistent and well defined sequence of events is used for different operations. These include pumpdown as described above and venting, opening up control of the vacuum system to the non-expert.

IV. INITIAL TESTS

Initial functional tests included test pumpdown and leak test to ensure that a useable vacuum could be reached as quickly as possible. A pressure of $\sim 1 \times 10^{-6}$ mbar is achieved after 20 min reaching $\sim 1 \times 10^{-7}$ mbar within an hour. Tests of the sample heater showed rapid heat up and cooldown possibilities, requiring approximately 20 min to stabilise once the correct control parameters had been established. Test depositions were made with the sample held at room temperature, where the evaporation rates measured using the QCM's were calibrated for samples deposited for a known amount of time and subsequently measured *ex situ* using laboratory based X-ray diffraction (see S1 in the supplementary material). The film thickness for the sample grown at room temperature is in excellent agreement with the expected thickness, confirming that the flux rates from the QCMs are accurate. The alignment procedure was simulated prior to first experiments, and the range of motion of the samples was checked to establish the parameters such as the pivot point and angular ranges for depth profiling measurements. It is clear that the design goal of ±5° was easily achieved and more than enough to enable sample alignment and setting of the incidence X-ray angle.

After installation on the beamline, initial X-ray alignment tests were carried out. The sample was moved out of the beam path by retracting the hexapod to its lowest position, and checks were made that the direct beam passed through the chamber and hit the detector at an appropriate position. The in-vacuum pre-sample slits were aligned around the direct beam, and they were calibrated to ensure that when fully closed there was not any transmission of the X-rays. The beam size was then set to be 100 μm × 100 μm. The beam stop was aligned by driving it to its lowest level vertically and then scanning in the horizontal direction to find the position at which the direct beam was blocked. The vertical motion was then scanned to find the point of the beam stop so that it could be aligned appropriately and block just the direct beam. Tests were then made on the reproducibility of the positioning and the ability of the beam stop to block the full X-ray beam when all attenuation had been removed. The slit and beam stop assembly were shown to behave very well, limiting the background scatter on the detector.

V. FIRST RESULTS

The capabilities of the MINERVA chamber extend beyond probing growth dynamics during *in situ* deposition, enabling also the observation of freshly deposited films exposed to external stimuli. Such investigations provide potentially critical information otherwise inaccessible in laboratory settings, where thin films must be transferred to an inert ambient-pressure glove box or to air. These experimental limitations preclude the observation of thin film evolution from its pristine, as-deposited state when exposed to air or analyte-carrying gases. Such studies have become increasingly important

in the context of solvent annealing microstructural transformations,[29] organic semiconductor (OSC)-based sensors,[30] and OPV stability.[31] One frequently used molecule is bathophenanthroline (BPhen), which is typically used as a buffer or doped electron transport layer between the active layer organic absorber/emitter and the evaporated metal cathode, composed of materials such as aluminium. Although ubiquitous in a number of organic light emitting diode (OLED) and OPV architectures, few if any investigations of the microstructure of vacuum-deposited BPhen exist. We have investigated thin films of BPhen on silica, which is known to transform from a glass-like organic layer into a more opaque, translucent scattering film over the course of an hour.

Sublimation-purified BPhen (Luminescence Technology Corp., Taiwan) was evaporated onto glass substrates (Thin Film Devices, Inc., USA) that were cleaned following a standard procedure of sonication successively in 2.5% Hellmanex (Sigma Aldrich) in deionised water, deionised water, acetone, and 2-propanol and subsequently dried in a light stream of N_2, followed by surface cleaning under ultraviolet (UV) ozone for 10 min prior to loading in the chamber. The X-ray energy was tuned to 12.5 keV (wavelength λ = 0.992 Å), and the substrate was aligned using optical methods to accurately orient the sample along the direction of the beam. The reflected spot position was recorded as the sample was translated across the X-ray beam to level it in the orthogonal direction. To monitor the surface of the film while limiting the scattering from the bulk, the substrate was rotated such that the X-ray incidence angle was $\Theta = 0.071°$, well below both the glass critical angle $\Theta_{c,glass} = 0.152°$ and the BPhen critical angle $\Theta_{c,Bphen} = 0.127°$. Although the intensity at this shallow grazing angle is relatively low, we can achieve significant depth sensitivity, with a minimum effective penetration depth[32] given by $z_0 = \frac{1}{2}\sqrt{r_e \pi \rho}$, where r_e is the Thomson scattering length and ρ is the electron density of the compound. Assuming vacuum deposited Bphen is crystalline, with an orthorhombic crystal structure[33] ($a = 7.253$ Å, $b = 10.810$ Å, $c = 21.14$ Å), the penetration depth $z_0 = 116$ Å which is slightly larger than that reported for crystalline P3HT of 85 Å.[32] As a result, changes in the depth dependence of the crystallographic features with increasing film thickness can be monitored closely in films relevant for optoelectronic devices.

The aim of the study was to investigate BPhen using the parameter space accessible with MINERVA, initially by monitoring the growth of a 40 nm thin film of BPhen and observing its evolution while under vacuum. Figure 6(a) shows the real-time deposition rate and thickness measured during growth with 2D GIWAXS images recorded at key points shown in Figs. 6(b) and 6(c). The appearance of powder rings in films of thickness greater than 10 nm indicates an isotropically growing film with negligible preferential vertical ordering. Using these images as a guide, radial regions of interest were defined and applied to all images acquired during *in situ* deposition, resulting in the plots shown in Fig. 7. These profiles show that in-plane ordering occurs in films of thickness as low as 2 nm, as evidenced by the appearance of two closely spaced peaks at $q_{xy} = 0.61$ Å^{-1} and 0.62 Å^{-1}. These features correspond to spacings of 10.13–10.30 Å, which are relatively close to the previously reported values for the **[010]** spacing of 10.4 Åin solution-growth BPhen crystals.[34] Notably, both these peaks shift to slightly higher q values with increasing thickness, suggesting that BPhen may exhibit closer in-plane packing when grown on itself as compared to on bare glass. As the film grows to nearly 40 nm thickness, new scattering features are observed at $q_{xy} = 1.11$ Å^{-1} and 1.19 Å^{-1}, respectively, indicating the concomitant development of in-plane scattering features.

After deposition, images were recorded while the X-ray incidence angle was varied from 0.073° to 0.153° (0.01° increment) to evaluate any depth-dependence in the crystallinity of the sample. Radial regions of interest identical to those shown in Fig. 7 were applied to the images, with results plotted in Fig. 8. The large change in penetration depth between the initial and final incidence angles provides information about the internal microstructure as a function of depth from the surface.

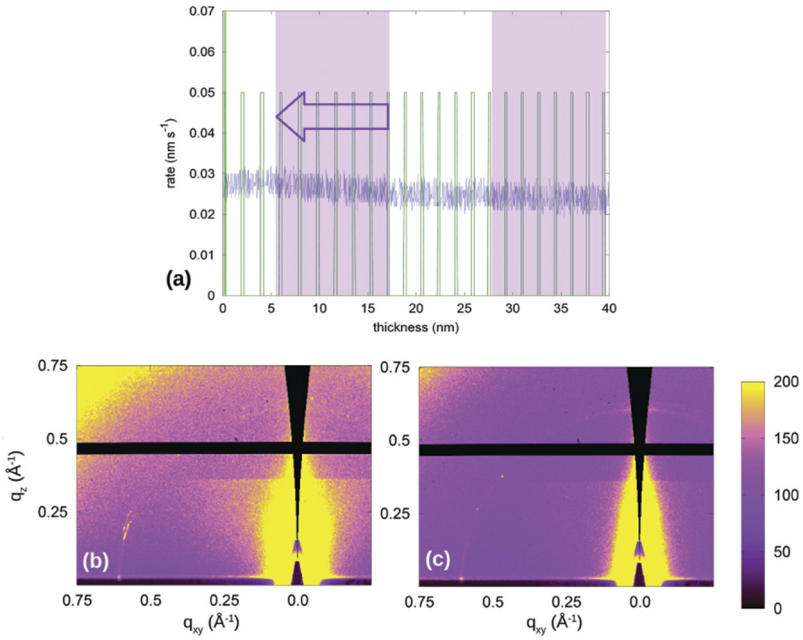

FIG. 6. *In situ* monitoring of BPhen grown on glass. (a) Recorded quartz crystal monitor (QCM) readout during BPhen deposition (blue) indicating a rate of 0.25–0.3 Ås^{-1}. Green step function denotes 10 s detector exposure time and shaded regions with arrows indicate the upper 11.6 nm probed in a given image based on the penetration depth into the film at 12.5 keV. Lower panels show GIWAXS images monitoring the 001 features after total growth time and film thickness of (b) 700 s, 17.5 nm and (c) 1470 s, 39 nm.

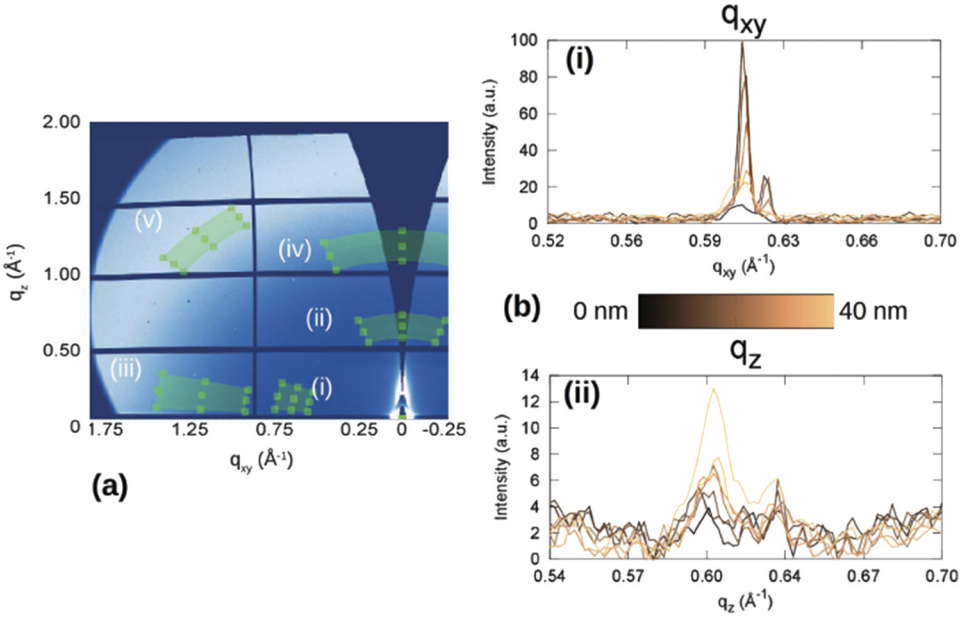

FIG. 7. Monitoring growth of BPhen grown on glass at rates of 0.25–0.3 Ås^{-1}. (a) Radial regions of interest (i-v) and (b) profiles from 2D detector images. Linear colorbar denotes the total film thickness at which each image was acquired during deposition [cf. Fig. 6(a)].

Several of the higher order q peaks, corresponding to the **020** and **002** features at 1.21 Å^{-1}, are clearly resolved at the highest penetration depth. A striking contrast with Fig. 7 is that the in-plane low-q features no longer appear as two separate peaks but are convoluted, with only a small shoulder near 0.62 Å^{-1}. It is the superposition of the q-shifted peaks of the various 11.6 nm slices of the film observed in Fig. 7 which results in this smearing of a single peak with only a shoulder at 0.62 Å^{-1}. By comparison, the same range along q_z reveals a more complex depth-dependence of the features; upper layers show a single

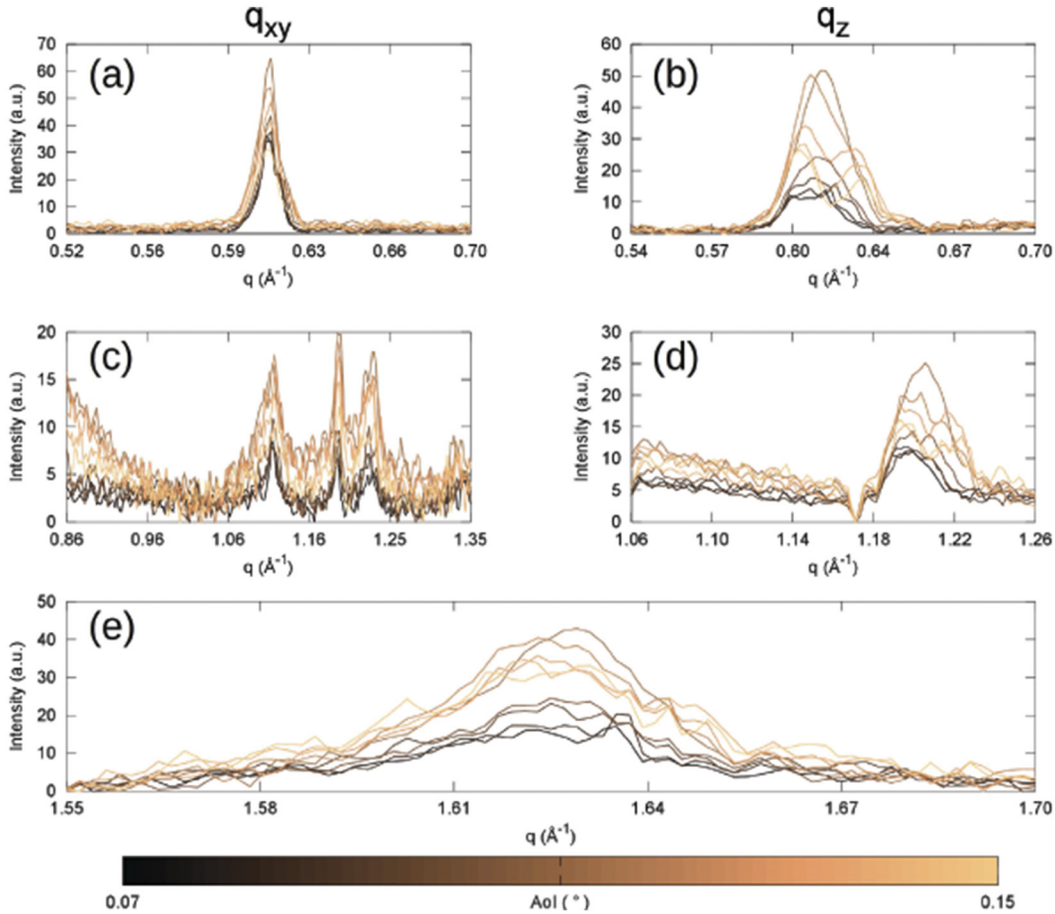

FIG. 8. Angle of incidence dependent region of interest profiles for a 40 nm BPhen film on glass. The variation in penetration depth ranges from 11.6 nm at $\Theta = 0.071°$ to the full 40 nm film thickness at $\Theta = 0.15°$, with the full film probed at $\Theta = 0.13°$.

broad peak with larger lattice spacing, while the layers in the lower half of the film exhibit two separate peaks, with lattice spacings larger and smaller, respectively, than at the surface. The larger spacing at shallower angles suggests a degree of surface relaxation in BPhen, a phenomenon observed in other crystalline organic semiconductors.[35] Although the evaporation rate varied only 10% (see Fig. 6), we cannot entirely rule out that the slightly higher evaporation rate (0.28 $Å s^{-1}$ vs 0.25 $Å s^{-1}$) during the first few nm of the deposition could lead to a kinetically constrained lower layer at the glass interface (with a different microstructure), as could the OSC "wetting layer" polymorphism observed in systems such as pentacene.[36] The temperature- and rate-dependence of such trapping, as well the influence of surface energy on BPhen arrangement, will be the subject of future studies with MINERVA.

The observed surface relaxation in the post-deposition scan of the BPhen film, coupled with the material's relatively low sublimation temperature of 140 °C, suggests that some of the rapid crystallisation seen in air may already occur to a limited degree under vacuum. To probe this behaviour, the thin film was maintained at 24 °C under vacuum in the deposition chamber ($P = 6 \times 10^{-7}$ mbar) and monitored at various time steps. Comparison of the radial profiles (Fig. S2 in the supplementary material) demonstrates a clear increase in scattering intensity for all of the scattering features, consistent with increased crystallisation of the film. Notably, comparison of the q_z features near the 001 peak indicates a slight relaxation within the upper part of the film, with the lattice spacing in this layer (corresponding to dark lines) shifting by +0.05 Å, while the layers near the glass substrate remain unchanged. Additionally, we can more clearly resolve the peak splitting in the 002 features for the film near the glass interface, as well as the emergence of a higher order powder ring at 1.69 $Å^{-1}$.

Comparison of the radial profiles for samples kept under vacuum reveals that the film undergoes greater out-of-plane reorganisation than in-plane, with the upper surface showing an increase of nearly 0.08 Å between initial deposition and the scan 2 h later. In addition to the changes with time, all samples show a small but systematic decrease in the lattice constant as the greater depth of the film is probed, as shown in Figs. 9(a) and 9(b). This change becomes significantly larger at an incidence angle of 0.13°, where the X-ray penetration depth is equal to the film thickness. At these higher angles, the out-of-plane layer spacing (derived from the [001] peak position) diverges into two separate peaks. The larger dimension corresponds to a lattice spacing of 10.39 Å, very close to the 10.40 Å value found by Mazumdar *et al.*,[34] but smaller than 10.81 Å identified by Ceolin *et al.*[33] The smaller of the two lattice constants is 9.97 Å, considerably smaller than previously reported values. Given that this large difference in q close to the specular beam arises when we reach the critical angle of the substrate, one possibility is that this distortion is due to refraction at the vacuum/film interface.[37,38] However, in that case, Δq_z would be expected to be of order ≤ 0.005 $Å^{-1}$ and so does not account for the large separation of the two q_z values. Alternatively, the presence of more than one peak when the sample is fully illuminated is most likely due to the presence of several close families of the BPhen crystal structure with different out-of-plane strain in the layers close to the interface, a hypothesis supported by the additional peaks near the [002] position (Figs. S2 and S3 in the supplementary material) which do not exhibit any peak splitting above the critical angle of the glass. Together with the absence of any change in q_{xy} with increasing time as seen in Fig. 9(a), these data suggest that the structure of nanocrystalline BPhen may accommodate greater reordering along the out-of-plane [00l] direction than along other planes, likely arising from the steric hindrance imposed by its two phenyl rings.

One key aspect of the MINERVA chamber is the ability to track the evolution of crystalline features with time, either during growth or under vacuum. Figure 10 shows such an evolution for the [001] peak, with initial time points corresponding to monitoring the upper surface during *in situ* growth and the final three-time points when kept under vacuum, post-deposition. In the case of the [001] peak, the relaxation of the upper surface with time can be compared against the steady-state growth of the film. Of note is the appearance of the [001] peak during the last few minutes of the film growth. This increased scatter from the [001] peak might arise from preferential out-of-plane growth, but it is also likely to arise from an increase in film roughness which results in a lower film density and hence a greater effective X-ray penetration depth probing *out-of-plane* scatter. Closer examination of Fig. 7 reveals that the film scatters highly in the *in-plane*

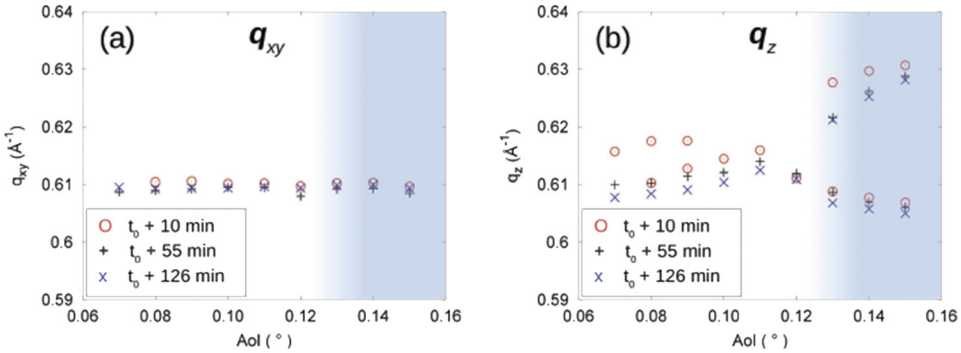

FIG. 9. Comparison of [010] and [001] evolution under vacuum at room temperature. Different symbols represent the time elapsed following the final deposition as indicated in the legend. (a) Radial RoI along q_{xy} and (b) along q_z, showing the presence of a layer with different out-of-plane ordering near the substrate interface. In-plane alignment does not change significantly while holding the sample under vacuum, while vertical ordering exhibits a greater change near the free surface. The shaded region indicates the angle at which the penetration depth of the X-rays exceeds the sample thickness.

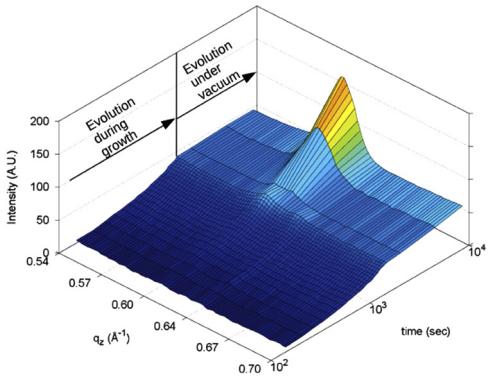

FIG. 10. Time series comparison of the [001] peak evolution. Earlier, closely spaced time points correspond to *in situ* measurements of the growing upper surface. The final three time points relate to the post-growth measurements illustrated in Fig. 9(b). In all cases, the angle of incidence was $\Theta = 0.07°$.

direction at low thickness, while it scatters more in the *out-of-plane* direction at higher thickness, suggesting that accumulation of orientational disorder during film growth is partly responsible for the observed coarsening of the film surface along the [001] direction.

VI. SUMMARY

A new facility (MINERVA, a facility to study Microstructure and INterface Evolution in Realtime under VAcuum) for use on the synchrotron beamline I07 at Diamond Light Source has been built for *in situ* monitoring of GIWAXS/GISAXS measurements during growth of vacuum deposited materials or modification of the environment in which the thin films are studied. The chamber allows co-evaporation of two materials and is configured to reduce the X-ray background, essential to monitor the scattering from, e.g., weakly scattering organic molecules. We have successfully demonstrated the parameter space accessible by MINERVA to observe the *in situ* nucleation and growth of a nanocrystalline BPhen thin film and observed how the nanocrystals coarsen with time at room temperature under vacuum. Our measurements reveal that BPhen, a common electrode interface material, undergoes minor but continuous surface relaxation relative to the bulk of the film when not covered by metal even in vacuum. Although a simple model system, these findings underscore the need to employ *in situ* methods to probe the effect of thin film fabrication conditions on the OSC microstructure, not only for the fabrication of high performance and stable devices but also to understand the degree to which measurements carried out even under vacuum (e.g., XPS/UPS[39]) on samples at long times after deposition can be related to the rapidly processed, device-relevant thin films used in large-scale production facilities. Furthermore, MINERVA opens the door for a wide variety of investigations of structure-property relationships involving vacuum deposited materials and their applications in optoelectronic and energy-related devices.

SUPPLEMENTARY MATERIAL

See supplementary material for calibration data used to determine the accuracy of the flux rates. Also included are data showing how the BPhen crystal structure develops as a function of film thickness and with time in vacuum.

ACKNOWLEDGMENTS

C.N., M.R., and J.M.H. were responsible for the initial design concept and overall management of the project. M.B., S.G., J.N., A.D., D.W., S.D., and A.W. detailed the design of the components and were responsible for assembly. All authors contributed to writing the manuscript under the coordination of C.N. We gratefully acknowledge funding to develop the chamber through the STFC Challenge Led Applied Systems Programme (CLASP) under Grant Nos. ST/L006294/1, ST/L006219/1 and access to Diamond beamtime at I07 under experiments Nos. SI14220-1 and SI15207-1. M.R. gratefully acknowledges funding through an EU FP7 Marie Curie Career Integration Grant (No. PCIG14-GA-2013-630864). We thank Simon Lay, Hugo Shiers, and Matthew Barnes (Diamond Light Source) for their work implementing the vacuum control and logic.

[1] F. Knudsen, J. Am. Ceram. Soc. **42**, 376 (1959).
[2] A. Wittstock, V. Zielasek, J. Biener, C. Friend, and M. Baeumer, Science **327**, 319 (2010).
[3] C. Poelking, M. Tietze, C. Elschner, S. Olthof, D. Hertel, B. Baumeier, F. Würthner, K. Meerholz, K. Leo, and D. Andrienko, Nat. Mater. **14**, 434 (2014).
[4] M. Schwarze, W. Tress, B. Beyer, F. Gao, R. Scholz, C. Poelking, K. Ortstein, A. Günther, D. Kasemann, D. Andrienko, and K. Leo, Science **352**, 1446 (2016).
[5] M. Jørgensen, K. Norrman, S. Gevorgyan, T. Tromholt, B. Andreasen, and F. Krebs, Adv. Mater. **24**, 580 (2012).
[6] M. Riede, T. Mueller, W. Tress, R. Schueppel, and K. Leo, Nanotechnology **19**, 424001 (2008).
[7] Y. Han, S. Meyer, Y. Dkhissi, K. Weber, J. Pringle, U. Bach, L. Spiccia, and Y.-B. Cheng, J. Mater. Chem. A **3**, 8139 (2015).
[8] D. Mastrogiovanni, J. Mayer, A. Wan, A. Vishnyakov, A. Neimark, V. Podzorov, L. Feldman, and E. Garfunkel, Sci. Rep. **4**, 4753 (2014).
[9] M. Hermenau, M. Riede, K. Leo, S. Gevorgyan, F. Krebs, and K. Norrman, Sol. Energy Mater. Sol. Cells **95**, 1268 (2011).
[10] A. Distler, T. Sauermann, H.-J. Egelhaaf, S. Rodman, D. Waller, K.-S. Cheon, M. Lee, and D. Guldi, Adv. Energy Mater. **4**, 1300693 (2014).
[11] B. Krause, S. Darma, M. Kaufholz, H.-H. Gräfe, S. Ulrich, M. Mantilla, R. Weigel, S. Rembold, and T. Baumbach, J. Synchrotron Radiat. **19**, 216 (2012).
[12] R. Döhrmann, S. Botta, A. Buffet, G. Santoro, K. Schlage, M. Schwartzkopf, S. Bommel, J. Risch, R. Mannweiler, S. Brunner, E. Metwalli, P. Müller-Buschbaum, and S. Roth, Rev. Sci. Instrum. **84**, 43901 (2013).
[13] S. Couet, T. Diederich, K. Schlage, and R. Röhlsberger, Rev. Sci. Instrum. **79**, 93908 (2008).
[14] S. Kowarik, J. Phys. Condens. Matter. **29**, 43003 (2017).
[15] D. Fong and C. Thompson, Annu. Rev. Mater. Res. **36**, 431 (2006).
[16] K. Ritley, B. Krause, F. Schreiber, and H. Dosch, Rev. Sci. Instrum. **72**, 1453 (2001).
[17] B. Jenichen, W. Braun, V. Kaganer, A. Shtukenberg, L. Däweritz, C.-G. Schulz, K. Ploog, and A. Erko, Rev. Sci. Instrum. **74**, 1267 (2003).
[18] A. Amassian, T. Desai, S. Kowarik, S. Hong, A. Woll, G. Malliaras, F. Schreiber, and J. Engstrom, J. Chem. Phys. **130**, 124701 (2009).
[19] K. Chou, B. Yan, R. Li, E. Li, K. Zhao, D. Anjum, S. Alvarez, R. Gassaway, A. Biocca, S. Thoroddsen, A. Hexemer, and A. Amassian, Adv. Mater. **25**, 1923 (2013).
[20] M. Sanyal, B. Schmidt-Hansberg, M. Klein, A. Colsmann, C. Munuera, A. Vorobiev, U. Lemmer, W. Schabel, H. Dosch, and E. Barrena, Adv. Energy Mater. **1**, 363 (2011).
[21] F. Bokel, S. Engmann, A. Herzing, B. Collins, H. Ro, D. DeLongchamp, L. Richter, E. Schaible, and A. Hexemer, Chem. Mater. **29**, 2283 (2017).

[22]H. Ro, J. Downing, S. Engmann, A. Herzing, D. DeLongchamp, L. Richter, S. Mukherjee, H. Ade, M. Abdelsamie, L. Jagadamma, A. Amassian, Y. Liu, and H. Yan, Energy Environ. Sci. **9**, 2835 (2016).
[23]C. Nicklin, T. Arnold, J. Rawle, and A. Warne, J. Synchrotron Radiat. **23**, 1245 (2016).
[24]V. Körstgens, J. Wiedersich, R. Meier, J. Perlich, S. Roth, R. Gehrke, and P. Müller-Buschbaum, Anal. Bioanal. Chem. **396**, 139 (2010).
[25]H. Proehl, R. Nitsche, T. Dienel, K. Leo, and T. Fritz, Phys. Rev. B **71**, 165207 (2005).
[26]R. Forker, M. Gruenewald, and T. Fritz, Annu. Rep. Sect. C Phys. Chem. **108**, 34 (2012).
[27]M. Huss-Hansen, A. Lauritzen, O. Bikondoa, M. Torkkeli, L. Tavares, M. Knaapila, and J. Kjelstrup-Hansen, Org. Electron. **49**, 375 (2017).
[28]F. Liscio, C. Albonetti, K. Broch, A. Shehu, S. Quiroga, L. Ferlauto, C. Frank, S. Kowarik, R. Nervo, A. Gerlach, S. Milita, F. Schreiber, and F. Biscarini, ACS Nano **7**, 1257 (2013).
[29]G. Purdum, N. Yao, A. Woll, T. Gessner, R. Weitz, and Y.-L. Loo, Adv. Funct. Mater. **26**, 2357 (2016).
[30]C. Zhang, P. Chen, and W. Hu, Chem. Soc. Rev. **44**, 2087 (2015).
[31]F. Anger, T. Breuer, A. Ruff, M. Klues, A. Gerlach, R. Scholz, S. Ludwigs, G. Witte, and F. Schreiber, J. Phys. Chem. C **120**, 5515 (2016).
[32]T. Schuettfort, L. Thomsen, and C. McNeill, J. Am. Chem. Soc. **135**, 1092 (2013).
[33]R. Ceolin, M. Mariaud, P. Levillain, and N. Rodier, Acta. Cryst. B **35**, 1630 (1979).
[34]P. Mazumdar, D. Das, G. Sahoo, G. Salgado-Morán, and A. Misra, Phys. Chem. Chem. Phys. **16**, 6283 (2014).
[35]H. Morisaki, T. Koretsune, C. Hotta, J. Takeya, T. Kimura, and Y. Wakabayashi, Nat. Commun. **5**, 5400 (2014).
[36]T. Kakudate, N. Yoshimoto, and Y. Saito, Appl. Phys. Lett. **90**, 81903 (2007).
[37]X. Lu, K. Yager, D. Johnston, C. Black, and B. Ocko, J. Appl. Crystallogr. **46**, 165 (2013).
[38]M. Tate, V. Urade, J. Kowalski, T. Wei, B. Hamilton, B. Eggiman, and H. Hillhouse, J. Phys. Chem. B **110**, 9882 (2006).
[39]S. Olthof, J. Meiss, B. Lüssem, M. Riede, and K. Leo, Thin Solid Films **519**, 1872 (2011).